CW-AcousLen: A Configurable Wideband Acoustic Metasurface

Juan He[1], Jie Xiong[2], Weighang Hu[1], Chao Feng[13], Enjie Yao[1]
Xiaojing Wang[1], Chen Liu[1*], Xiaojiang Chen[134]
[1]Northwest University
[2]Microsoft Research Asia and University of Massachusetts Amherst
[3]Shaanxi International Joint Research Centre for the Battery-Free Internet of Things
[4]Xi'an Advanced Battery-Free Sensing and Computing Technology International Science and Technology Cooperation Base
Email: {hejuan, wxj}@stumail.nwu.edu.cn, {huweihang_nwu, yaoenjienwu}@163.com,
{chaofeng, liuchen, xjchen}@nwu.edu.cn, jxiong@cs.umass.edu

ABSTRACT

Acoustic metasurface was recently proposed to enhance the performance of acoustic communication and sensing. While promising, there are two issues hindering the adoption of acoustic metasurface for real-life usage. The first issue is that configurable metasurface is still expensive and unscalable. The second issue is that it is difficult for an acoustic metasurface to work in a large frequency range. In this paper, we present a wideband and configurable acoustic metasurface for the first time. We show that with a large number of metasurface elements, a cheap and simple two-state element design can achieve performance very close to that achieved by expensive continuous-state elements. We also fine-tune the geometric parameter of the element structure to support similar phase changes across a large frequency range, laying the foundation to enable wideband acoustic metasurface. Extensive experiments show that our system can achieve an average signal strength improvement of 7.5 dB and 10.5 dB in LoS and NLoS scenarios respectively with the help of a metasurface with a size of 17.6 × 17.6 *cm*. Two representative sensing applications (i.e., respiration sensing and gesture recognition) and one communication case study are employed to show the effectiveness of the metasurface.

CCS CONCEPTS

• **Hardware** → **Wireless devices**; • **Networks** → *Physical links.*

KEYWORDS

Acoustic Metasurface, Configurable Environment, Wideband Beamforming, Acoustic Sensing.

ACM Reference Format:
Juan He[1], Jie Xiong[2], Weighang Hu[1], Chao Feng[13], Enjie Yao[1] and Xiaojing Wang[1], Chen Liu[1*], Xiaojiang Chen[134]. 2024. CW-AcousLen: A Configurable Wideband Acoustic Metasurface. In *The 22nd Annual International Conference on Mobile Systems, Applications and Services (MOBISYS '24), June 3–7, 2024, Minato-ku, Tokyo, Japan.* ACM, New York, NY, USA, 13 pages. https://doi.org/10.1145/3643832.3661882

* Corresponding author.

Permission to make digital or hard copies of all or part of this work for personal or classroom use is granted without fee provided that copies are not made or distributed for profit or commercial advantage and that copies bear this notice and the full citation on the first page. Copyrights for components of this work owned by others than the author(s) must be honored. Abstracting with credit is permitted. To copy otherwise, or republish, to post on servers or to redistribute to lists, requires prior specific permission and/or a fee. Request permissions from permissions@acm.org.
MOBISYS '24, June 3–7, 2024, Minato-ku, Tokyo, Japan
© 2024 Copyright held by the owner/author(s). Publication rights licensed to ACM.
ACM ISBN 979-8-4007-0581-6/24/06…$15.00
https://doi.org/10.1145/3643832.3661882

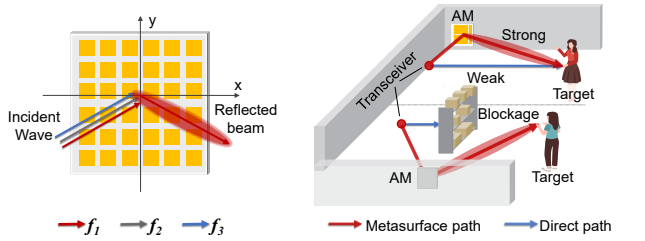

(a) Wideband beamforming **(b) LoS and NLoS sensing scenarios**

Figure 1: CW-AcousLen's metasurface can steer the wideband signal towards the target direction, improving the performance of acoustic sensing in both LoS and NLoS scenarios.

1 INTRODUCTION

Recent years have witnessed a rapid progress of applying metasurface to improve the performance of communication [11, 16, 27, 37] and sensing [2, 13, 15, 47]. Instead of devoting effort to the transmitter and receiver, metasurface explores the potential of manipulating the signal propagation environment to improve the performance of communication and sensing. A metasurface can reshape the incident wave by altering the phase or amplitude of signals and usually consists of many elements.

Among the metasurface designs, acoustic metasurface attracted a tremendous amount of attention owing to the widespread of acoustic modules (i.e., speakers and microphones) in our surrounding environment. Different from RF metasurface which employs diodes and varactors to vary the signal phase, acoustic signal is a mechanical wave and the phase is varied by guiding acoustic signal to propagate through carefully designed structures such as curved channels to vary the propagation path length. However, the mechanical structures usually are non-configurable. This results in poor adaptability to environmental changes and signal changes such as signal frequency change.

To enable configurability, the state-of-the-art design [51] uses a speaker array and leverages the configurability of the speaker array to enable beam-steering with metasurface. This design requires the speaker array and the metasurface to be placed extremely close to

each other, i.e., 2 cm [51]. This proximity makes the metasurface almost part of the transmitter, losing the original objective of metasurface, i.e., programming the environment to enhance signal strength. On the other hand, active acoustic metasurfaces with the capability of reconfiguration are expensive [6, 9, 31]. A single element usually costs tens of dollars, which are not scalable. Another issue associated with acoustic metasurface is that it works in a relatively small frequency range. However, chirp signals are widely employed in acoustic sensing and communication to improve sensing resolution and communication throughput [5, 8, 16, 22, 25, 30, 48]. Existing acoustic metasurfaces do not work effectively when the incoming signal is a chirp spanning across a large frequency band or consists of multiple single frequencies separated far away. This is because metasurface relies on manipulating signal phase to constructively combine signals. Phase values vary with frequencies and it is thus challenging for a fixed design to work in a wide frequency range.

In this paper, we aim to enable configurability at low cost and make acoustic metasurface work in a large frequency range, pushing acoustic metasurface one step forward towards real-life adoption. To make the metasurface configurable at a low cost, we adopt a very simple two-state design at each element. This two-state design is based on one key observation that with a large number of metasurface elements, the gap between continuous element states and a small number of discrete element states (e.g., two states) is quite small. For example, for a metasurface with 144 elements (i.e., 12×12), with just two states at each element, the achieved beamforming direction deviation is less than 1° and the gain is only around 3 dB lower compared to that achieved with infinite number of continuous states. Thus, by leveraging the inherent advantage of large number of elements at a metasurface, even the simplest two-state design can realize fine-grained beam patterns. This observation helps significantly reduce the complexity of hardware design and accordingly the cost of the configurable (active) metasurface.

To enable acoustic metasurface working in a large frequency range, we adopt the Helmholtz resonator structure [6, 54] as the basic metasurface element. We leverage one key observation that the Helmholtz resonator exhibits similar phase changes across different frequencies if we carefully tune the geometry of the basic element [6], laying the foundation of enabling acoustic metasurface working in a wide frequency range. To make it happen, we model the relationship between the phase change and the geometry of the basic element. Based on the model, we formulate our objective as an optimization problem to derive the optimal geometric parameters. With our design, we ensure the same phase change (e.g., 180 degrees) is induced when the same mechanical state change of the metasurface element is applied (e.g., from plunger pushed in to pulled out) at different frequencies. This significantly reduces the computational complexity when we design the coding pattern (i.e., the 0/1 states for all the elements) for beamforming. To support wideband beamforming, the objective is to find a common coding pattern that can achieve high beamforming gain not just at one single frequency but across the entire inaudible band (i.e., 16 kHz - 24 kHz). While the optimal coding patterns at different frequencies are different, we notice that they share a large number of common-state elements. This insight inspires us to reduce the computational complexity by only optimizing the remaining elements for the common coding pattern.

We prototyped the proposed configurable acoustic metasurfaces with 16×16 elements using resin materials. Each element is 3D printed and we employ cost-effective solenoid valves to control the mechanical movement of the plunger inside each element. Each metasurface element costs around $0.35. An FPGA-based control module is used to configure the metasurface rapidly within 0.02 s.

Comprehensive experiments demonstrate that even with a small-size prototype ($17.6\ cm \times 17.6\ cm$), our system can achieve an average signal strength improvement of 7.5 dB in Line-of-Sight (LoS) and 10.5 dB in Non-Line-of-Sight (NLoS) scenarios, respectively. By applying the configurable metasurface to a speaker array, the beamforming coverage can reach almost 360°. We showcase the effectiveness of the proposed metasurface using two representative acoustic sensing applications, i.e., human respiration sensing and gesture recognition. In LoS scenarios, the mean sensing accuracy can be increased by 20% for hand gestures and the median respiration sensing error is decreased from 1.32 to 0.46 bpm (beats per minute). Even in challenging NLoS scenario, with the help of the proposed acoustic metasurface, our system can significantly extend the sensing range to 3 m for gesture recognition. Note that in NLoS scenarios, the signal is reflected at least twice before reaching the receiver, which is too weak to be utilized for sensing without the help of a metasurface.

Contributions. To summarize, we present CW-AcousLen, a low-cost configurable acoustic metasurface capable of working in a wide frequency range. Compared to the state-of-the-art design which requires a speaker array, the proposed metasurface design can work with a single speaker. Through deeply understanding the principle, we show that a two-state simple design can achieve comparable performance as those designs employing continuous states which are expensive and unscalable. We implement a real-time control mechanism including both hardware and software designs that can quickly configure the metasurface for beamforming. We fabricate a prototype of the proposed acoustic metasurface and validate its effectiveness using sensing and communication applications in real-world environments.

2 RELATED WORK

Acoustic metasurfaces. A lot of acoustic metasurface designs have been proposed recently to enhance the performance of communication [43, 46] and sensing [2, 15, 51]. Most designs achieve phase control by guiding acoustic waves to propagate through dedicated structures such as curled channels [2, 15, 29, 40, 51, 53]. These designs are not configurable. To enable configurability, the state-of-the-art design [51] uses a speaker array co-located with a non-configurable metasurface to enable beam-steering. A lot of efforts were also devoted to active (i.e., configurable) acoustic metasurfaces. Recent works [6, 38, 49] adopt expensive mechanical structures with step motor, driver, and controller in each single element. Other works [4, 9, 31] use advanced materials that can be deformed under the fine control of magnetic field, together with a large number of complex relay modules. Furthermore, some works [35, 36] propose the concept of piezoelectric-based structure that varies phase using electric current. However, the piezoelectric-based design has a low power efficiency, i.e., more than 50% power loss. In contrast, CW-AcousLen enables configurability at low cost (i.e.,

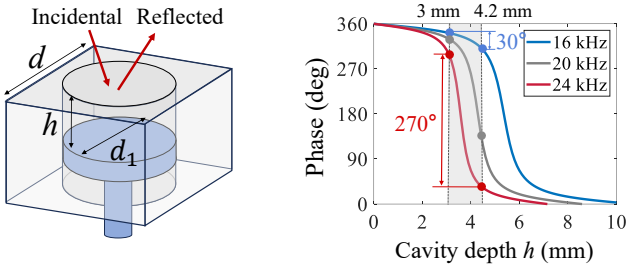

(a) Basic Helmholtz resonator structure. **(b) Inconsistent phase changes across different frequencies.**

Figure 2: The Helmholtz resonator structure with one cavity.

each element costs just $0.3) and the power efficiency is high (i.e., 90%).

Wideband design. Some effort has been devoted to designing wideband metasurfaces. The straightforward solution is to combine multiple sub-structures with each operating in a specific frequency range [42, 45, 52]. While effective, such solution increases both the physical size and the complexity of the hardware design. Another work [12] adopts a helical structure to enable continuous phase shift between 0 and 2π, supporting a wideband frequency range. However, it requires delicate mechanical control at each element to support a large number of states, making the design complicated and less practical for real-world adoption. In contrast, CW-AcousLen utilizes the simplest two-state valve for element control. The supported bandwidth is 8 kHz (i.e., 16-24 kHz) which mainly focuses on sensing. The state-of-the-arts [51] support a bandwidth of 2 kHz in the angular range of [-60°, 60°].

Speaker/microphone array. One common strategy to improve signal's SNR is to use a speaker or microphone array [23, 25, 30, 33, 44]. Although promising, a lot of commodity devices still have just 1-2 speakers, resulting in a limited SNR improvement. In addition, speaker arrays have a small angular range. CW-AcousLen requires just a single speaker to work and the metasurface design can enable not just longer sensing range but a wider angular coverage.

RF metasurfaces. Numerous metasurfaces operating in the radio signal frequency (RF) band have been proposed. By controlling the phase, amplitude, and polarization of the incident signal, RF metasurfaces can change the propagation properties of electromagnetic waves. By deploying metasurfaces to alter ambient wireless signals, an intelligent environment can be created to facilitate communication [7, 10, 26, 27, 32, 50] and sensing [13, 47]. For example, RFlens [13] proposed a metasurface working in 5G Wi-Fi bands to enable beamforming for low-cost IoT devices. RF-Bouncer [27] designed a dual-band (i.e., 2.4-2.48 GHz and 5.15-5.35 GHz) metasurface for communication. However, compared to the gigahertz carrier frequency, the supported bandwidth is still narrow band. The optimization scheme proposed in these designs can not be applied to our case. CW-AcousLen proposes both hardware and software designs to make wideband acoustic metasurface work.

3 HARDWARE DESIGN

In this section, we detail the hardware design of our metasurface, including the design of the individual element and the overall architecture of the metasurface system.

3.1 Design Goals and Challenge

Design goals. To support a wideband range, we have the following two goals for CW-AcousLen's element design: *(1) Consistent phase shift in a wide frequency range.* We would like to ensure that for a same mechanical state change (e.g., 0->1), the phase change is consistent across the targeted wide frequency range (e.g., 16-24 kHz). This requirement does not mean the absolute phase values are identical, but rather that the phase difference remains consistent. For example, 0° to 180° and 10° to 190° represent the same phase change. *(2) High reflection efficiency.* The signal gets through the element structure with a small power loss.

Challenge. For acoustic signal, phase change is typically achieved through varying the signal propagation path. However, such approaches result in *frequency-dependent phase response*: signals at different frequencies experience different amounts of phase shifts when traversing the same path.

3.2 Element Design

3.2.1 Enabling metasurface element with the same phase change in a wide frequency range. We propose to build CW-AcousLen's element based on the Helmholtz resonator structure [54]. This structure can be 3D printed at a low cost. Typically, a Helmholtz resonator consists of multiple cavities with different sizes. Here, we first consider a simple Helmholtz resonator with just one cavity. As shown in Figure 2a, it consists of a square cube with a cylindrical cavity. The cube has a side length of d, while the cavity has a diameter of d_1 and a depth of h. The key to manipulating the phase shifts lies in varying the depth (h) of this cavity. Specifically, by altering h, the incidental signals traverse different depths before being reflected from the bottom layer of the cavity, resulting in different phase shifts. However, the phase shifts are different as signal frequency varies. As shown in Figure 2b, for the same cavity depth change from 3 mm to 4.2 mm, the phase changes for 16 kHz, 18 kHz, and 24 kHz are dramatically different.

To support a wide frequency range, it is critical to ensure that the same change in the cavity depth (h) leads to relatively consistent phase changes across different frequencies. To analyze the relationship between the phase shift and the cavity depth (h), we model the Helmholtz resonator structure as a cascaded two-port network [55]. This model allows us to analyze the signal transmission characteristics within the structure. The reflection coefficient Γ can be calculated as:

$$\Gamma = \frac{-{d_1}^2/d^2 cos(\frac{2\pi f}{c}h) + jsin(\frac{2\pi f}{c}h)}{{d_1}^2/d^2 cos(\frac{2\pi f}{c}h) + jsin(\frac{2\pi f}{c}h)} = e^{-j2arctan\frac{tan(\frac{2\pi f}{c}h)}{{d_1}^2/d^2}}, \quad (1)$$

where c is the sound velocity in air and f is the frequency of the incident signal. The phase shift is characterized by the complex reflection coefficient Γ and can be expressed as:

$$\varphi = 2arctan\frac{tan(\frac{2\pi f}{c}h)}{{d_1}^2/d^2}. \quad (2)$$

The above equation reveals that the phase shift φ, related to the cavity depth (h), is influenced not only by the frequency of the incident signal but also by the ratio d_1/d. This observation presents an opportunity to decouple the phase shift and its frequency dependency by carefully tuning the ratio d_1/d. That is to say, with

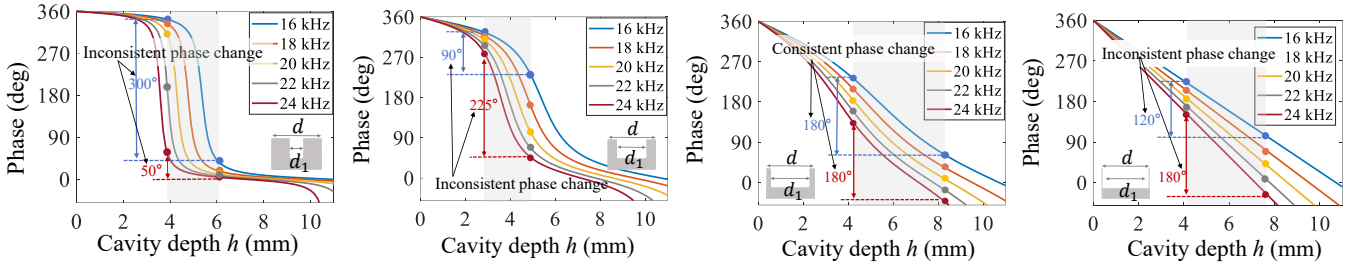

(a) $d_1/d = 0.3$ **(b)** $d_1/d = 0.6$ **(c)** $d_1/d = 0.95$ **(d)** $d_1/d = 1$

Figure 3: The phase change with respect to the cavity depth h across different frequencies can be tuned by varying d_1/d.

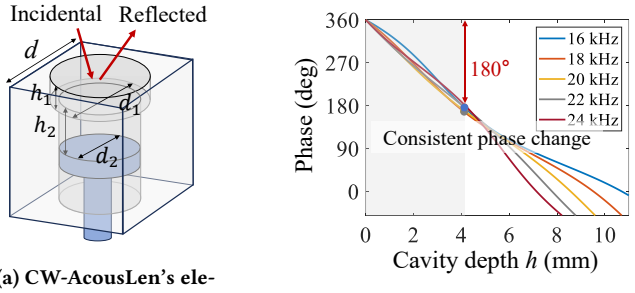

(a) CW-AcousLen's element structure design. **(b) The optimized phase change.**

Figure 4: The CW-AcousLen's element structure design and the optimized phase curve across different frequencies.

a properly chosen value of d_1/d, the same change in cavity depth (h) can result in consistent phase changes across different frequencies. This concept is demonstrated in Figure 3, which presents the COMSOL [1] simulation results for various d_1/d ratios, with the frequency of the incident signal varied between 16 and 24 kHz. Notably, as shown in Figure 3c, when d_1/d is set to 0.95, consistent phase changes are observed across all frequencies as the cavity depth (h) changes from 4.2 to 8.2 mm. For instance, at 16 kHz, the phase varies from 240° to 60°, resulting in a 180° phase shift. At 24 kHz, the phase changes from 135° to -45°, also presenting a 180° phase shift. These results verify the effectiveness of decoupling the dependency of phase shift on frequency by tuning the value of d_1/d. However, a problem occurs when a single cavity design with the optimal ratio of $d_1/d = 0.95$ is adopted. For instance, if $d = 10\ mm$, d_1 would be 9.5 mm, resulting in a wall thickness of just 0.25 mm for the Helmholtz resonator structure. This thinness makes the wall lose the rigidity required for our model derivation, as the rigidity of the cavity wall is a prerequisite condition in the model [21, 55]. The lack of rigidity can introduce complex acoustic wave coupling and increased reflection losses.

Decouple the dependency of phase shift on frequency by introducing additional cavities. To address the problem encountered with single-cavity design, we propose to add additional cavities. Besides tuning the ratio of d_1/d, we can also adjust the ratios of other cavities to achieve the desired consistent phase change across various frequencies. However, incorporating too many cavities can lead to an increase of cavity depth, which results in signal attenuation [28]. To trade off attenuation, physical size, and wideband capability, we choose the structure with two cavities, as shown in Figure 4a. The reflection coefficient Γ for this two-cavity structure can be calculated as:

$$\Gamma = \frac{-(1+d_{21})[d_{10}cos(\frac{2\pi f}{c}h) - jsin(\frac{2\pi f}{c}h)] + (1-d_{21})}{(1+d_{21})[d_{10}cos(\frac{2\pi f}{c}h) + jsin(\frac{2\pi f}{c}h)] - (1-d_{21})} \frac{[d_{10}cos(\frac{2\pi f}{c}h') - jsin(h')]}{[d_{10}cos(\frac{2\pi f}{c}h') + jsin(\frac{2\pi f}{c}h')]}, \tag{3}$$

where $d_{10} = d_1/d$, $d_{21} = d_2/d_1$, $h = h_1 + h_2$, and $h' = h_2 - h_1$. The phase shift is obtained by calculating the angle of the reflection coefficient, i.e., $\varphi = arg(\Gamma)$. To achieve consistent phase changes across different frequencies, we jointly fine-tune the values of d_1/d and d_2/d_1. While determining the optimal parameters can be obtained with the help of the simulation tools such as COMSOL [1], it is extremely time-consuming. We therefore formulate it as an optimization problem.

Problem formulation. Specifically, for a given range of cavity depth (e.g., from h_s to h_e), if a particular configuration (d_1/d and d_2/d_1) can provide consistent phase changes across a broad frequency range, we consider the parameters of this configuration as "decoupling parameters". As illustrated in our previous analysis (see Figure 3c), achieving consistent phase changes over a wide frequency range implies that *the phase shift curves with respect to the cavity depth for different frequencies ($\varphi(f_i)$) appear as parallel lines.* This indicates that the rate of the phase change with respect to the cavity depth is constant for different frequencies. We denote the working frequency range as $F = \{f_1, f_2, ..., f_i, ..., f_n\}$ and the rate of phase change for each frequency can be calculated as $\frac{\partial\varphi(f_i)}{\partial(h)}$ based on Equation 3. Our objective is to find the geometric parameters (d_1/d and d_2/d_1) that can provide a same rate of phase change across different frequencies, which can be described as:

$$\underset{d,\, d_1,\, d_2,\, h_s,\, h_e}{arg\ min} \sum_{i=1}^{n} (\frac{\partial\varphi(f_i)}{\partial(h)} - \delta)^2, \tag{4}$$

where δ represents the common phase change rate. By solving this optimization problem, we can obtain the optimal parameters (d_1/d and d_2/d_1). For instance, in a frequency range between 16 and 24 kHz, the optimal d_1/d is 0.8 and d_2/d_1 is 0.78. To validate these theoretically derived parameters, we perform a simulation using COMSOL. Figure 4b shows the simulation results. We can see that with the derived optimal parameters, as the depth (h) varies

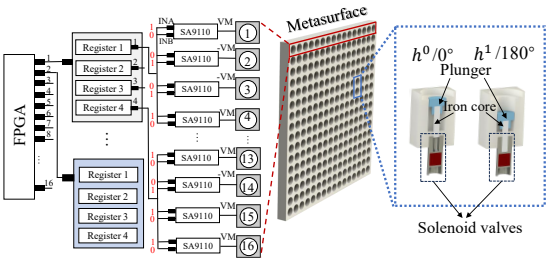

(a) CW-AcousLen's control architecture.

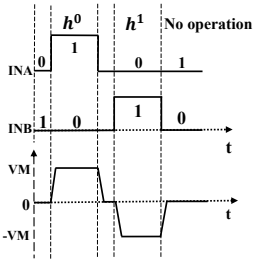

(b) Timing diagram.

Figure 5: Control mechanism: the plunger in each element can be switched between h^0 and h^1 with a low-cost FPGA.

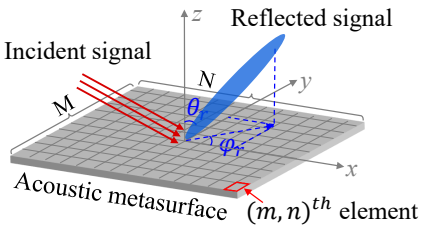

Figure 6: Geometry of the proposed acoustic metasurface.

from 0 to 4 mm, there exist consistent phase changes across all frequencies, represented by the approximately parallel lines.

3.2.2 High Reflection Efficiency. To achieve a high reflection efficiency, we further apply one step on our design. We select the material which can reflect more signal power back. Specifically, we would like to make the difference between material impedance and air impedance as large as possible. As the acoustic impedance of the material is determined by the multiplication of the material density and the acoustic velocity of the material, we choose a material (i.e., G-10CR resin) with high density and high acoustic velocity.

3.3 Metasurface Control

To enable configurability, prior works utilize a step motor [6, 38, 49] to achieve continuous phase shift at each element. This design becomes expensive when applied to metasurfaces with a large number of elements. CW-AcousLen, in contrast, introduces a cost-effective solution by adopting a 1-bit configuration with just two phase states. In the later section, we compare the performance of our 1-bit phase shift approach with the continuous phase shift method.

To realize configurability, CW-AcousLen employs low-cost solenoid valves ($0.3 each) to control the position of the plunger inside the element cavity. As shown on the right side of Figure 5a, the plunger, connected to the iron core inside the valve, is controlled by an electromagnet. By applying two different voltages, the solenoid valves can alternate between "push in" and "pull out", thereby switching the plunger's position between the h^0 and h^1 states. For example, applying a "10 V" voltage corresponds to the "h^0" state while a "-10 V" voltage shifts it to the "h^1" state, as shown in Figure 5b.

The controller for the entire metasurface. We build a metasurface prototype consisting of 16×16 elements, as shown in Figure 5a. To configure the entire metasurface, we designed a control circuit module that includes an FPGA controller and $M \times N$ DC driver chips (SA9110) to provide voltage control for the solenoid valves. Each DC driver chip costs approximately $0.05. The FPGA is programmed to output different combinations of "0/1" levels, which can control the SA9110 to deliver "10 V/-10 V" voltages. These voltages can control the position of the plunger in each element. CW-AcousLen utilizes a low-end FPGA to control the metasurface since it does not require much on-chip resource. As low-end FPGA (e.g., Xilinx Artix-7 XC7A35T [14] in our implementation) has a limited number of GPIO pins, we use 64 SN74HC595 [18] shift registers to expand the GPIO pin capacity, with each register costs around $0.05. Specifically, each channel connects four registers to store 32 bits of data. Once the enabled port of the shift register is triggered, a 32-bit data stream from each register controls 16 elements. This design allows independent configuration of each element's state. When all control signals are concurrently dispatched through 64 shift registers, the configuration latency for the entire 16 × 16 metasurface is about 20 ms.

4 BEAMFORMING

CW-AcousLen enables beamforming by configuring the phase state of each element. Specifically, our metasurface operates in two modes: *(1) Single-frequency mode,* and *(2) Wideband-frequency mode.* In the second mode, CW-AcousLen handles signals from a wide frequency range (i.e., 16 to 24 kHz for acoustic sensing).

4.1 Single Frequency Beamforming

We employ a metasurface consisting of $M \times N$ elements as shown in Figure 6 to illustrate the concept. When an acoustic wave impinge on the metasurface, the phase shift of each element is configured to achieve beamforming. Specifically, given the beamforming direction (θ_r, ϕ_r) and the frequency f_0 of the incident signal, the theoretical phase compensation of each element can be calculated as:

$$\varphi^C_{m,n} = k(mdsin\theta_r cos\phi_r + ndsin\theta_r sin\phi_r) - \varphi^I_{m,n}, \quad (5)$$

where $\varphi^I_{m,n} = kd_{m,n}$ is the phase delay caused by the propagation distance $d_{m,n}$ from the signal source to the $(m,n)th$ element. We have $k = 2\pi/\lambda$, where λ is the wavelength of the signal. The matrix $\boldsymbol{\Phi^C} = \{\varphi^C_{1,1}, \varphi^C_{1,2}, ..., \varphi^C_{m,n}\}$ is defined as the *coding pattern*, which is the set of phase states for all elements. Metasurfaces realize beamforming by controlling the phase difference between adjacent elements so that the reflected signals from these elements superimpose constructively.

Continuous Phase Shift vs. Discrete 1-bit Phase Shift. According to Equation 5, the ideal phase compensation is a set of continuous phase shifts. Implementing such continuous phase shift is highly expensive. To enable a cost-effective configurable metasurface, we employ a 1-bit state design. Specifically, each element acts as a 1-bit phase shifter, offering only two discrete phase states. To quantize continuous phase compensation into discrete states,

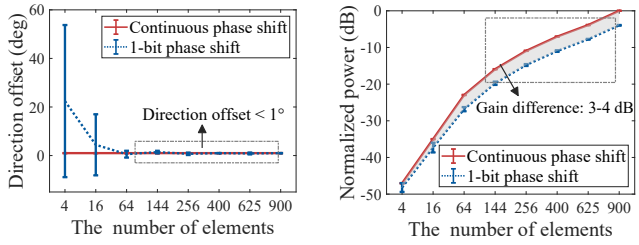

(a) Direction offset. (b) Gain difference.

Figure 7: (a) Direction offset: the angular difference between the desired direction and the actual direction of the main beam lobe. (b) Gain difference: power gain difference between the continuous phase coding pattern and the 1-bit phase coding pattern.

we apply the following quantization rule:

$$\mathrm{R}\left(\varphi^{C}_{m,n}|_{1-bit}\right) = \begin{cases} \pi, \ if \ \pi/2 \ \leq \varphi^{C}_{m,n} < 3\pi/2 \\ 0, \ \text{otherwise.} \end{cases} \tag{6}$$

The choice of 0 and π as the two 1-bit phase states is based on the Intermediate Value Theorem [19]. The adoption of 1-bit phase quantization would inevitably introduce phase errors and affect the beamforming performance. To investigate this impact, we analyze the performance gap between continuous and 1-bit phase shifts in terms of power gain and beamforming direction accuracy. The simulation results are shown in Figure 7. We can see that as the number of elements in the metasurface increases, the direction offset decreases and eventually approaches zero. The difference in power gain stabilizes at 3-4 dB. To summarize, even with just 1-bit state change (i.e., two states), a metasurface with a large number of elements (e.g., 256 elements in our implementation) can achieve the beamforming gain and target direction comparable to that achieved with continuous phase shifts.

To summarize, for single-frequency beamforming, the process involves first calculating the theoretical continuous phase coding pattern, followed by deriving the 1-bit coding pattern based on the quantization rule specified in Equation 6. By controlling the cavity depth h of each element, the metasurface can be configured to produce the desired coding pattern, generating the desired beam pattern.

4.2 Wideband Beamforming

Challenge. For wideband frequency, the coding patterns required by different frequencies are different. Unfortunately, the metasurface can only adopt one coding pattern at a time, making it challenging to achieve desired beam patterns for all frequencies in a large frequency range (e.g., a chirp signal).

Intuitively, we can use the coding pattern of the center frequency for the whole frequency range. Figure 8 shows the gain performance across different frequencies. In this simulation, we set the desired beamforming angle as 45° and calculate the 1-bit coding pattern for the center frequency (20 kHz) at this angle. We then apply this pattern to the entire frequency range (16 to 24 kHz). We can see that power drops at frequencies away from the center frequency. To address this problem, we propose a wideband beamforming algorithm.

Wideband optimization. Our goal is to drive a *coding pattern* $\boldsymbol{\Phi^*}$ that maximizes the total signal strength in the target direction (θ_r, ϕ_r) across the entire frequency band. Let $F = \{f_1, f_2, ..., f_i, ..., f_l\}$ represent l evenly distributed frequencies in the frequency range. Given a random 1-bit coding pattern $\boldsymbol{\Phi^C} = \{\varphi^{C}_{1,1}, \varphi^{C}_{1,2}, ..., \varphi^{C}_{m,n}\}$, the signal strength at the direction of (θ_r, ϕ_r) for frequency f_i can be calculated as:

$$G^{f_i}_{(\theta_r,\phi_r)} = \sum_{m=1}^{M}\sum_{n=1}^{N} a_{m,n} e^{j\left(k(mdu+ndv)-\varphi^{C}_{m,n}-\varphi^{I}_{m,n}\right)}, \tag{7}$$

where $a_{m,n}$ is the amplitude, $u = sin\theta_r cos\phi_r$, and $v = sin\theta_r sin\phi_r$. To maximize the total signal strength along direction (θ_r, ϕ_r) while maintaining consistently high strength across all frequencies, we define our objective function as:

$$\Phi = \underset{\boldsymbol{\Phi^*}}{arg\,min} \quad \underbrace{W_1 \sum^{f_i \in F} \left| G^{f_i *}_{(\theta_r,\phi_r)} - G^{f_i}_{(\theta_r,\phi_r)} \right|}_{maximize\ the\ total\ signal\ strength} + \underbrace{W_2 \sigma^2 (G^{f_i}_{(\theta_r,\phi_r)})}_{minimize\ the\ variance}, \tag{8}$$

where $G^{f_i *}_{(\theta_r,\phi_r)}$ is the theoretical maximum signal strength for single frequency f_i using continuous phase shifters. W_1 and W_2 are the weight coefficients, and σ is the variance. The first half maximizes the total signal strength across l frequencies and the second half minimizes the variance of the signal strengths across different frequencies to avoid a large signal strength discrepancy among frequencies. However, optimizing the above equation is challenging. For instance, directly applying the Particle Swarm Optimization (PSO) algorithm [20] might face the non-convergence issue due to a large number of elements and a wide frequency range.

We address the issue leveraging the following observations: *We observe that the optimal 1-bit coding patterns at different frequencies share a large portion of common element states.* Figure 11 shows an example of these common element states shared for all frequencies. By keeping these common states unchanged and only optimizing the remaining ones, we significantly reduce the search space. Also, *owning to the continuity of coding patterns across adjacent frequencies, there is no need to consider a large number of frequencies.* Instead, we just need to consider a few frequencies evenly distributed in the frequency range. Incorporating these observations leads to a reduction in both the number of frequencies and the number of elements we need to consider for optimization, effectively reducing the computational load.

Identify common element states across frequencies. The 1-bit coding patterns for different frequencies can be derived by combining Equation 5 and Equation 6. We would like to maximize the number of common-state elements across the frequency band, reducing the number of elements that need to be optimized. However, employing a same quantization boundary for all frequencies may not achieve this goal. We thus apply different quantization boundaries to each frequency to generate various coding pattern combinations. We then search for the set of quantization boundaries that yield the highest number of common-state elements across selected frequencies.

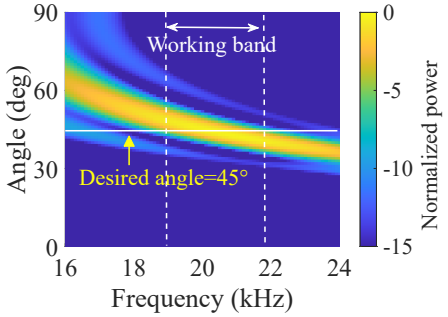

Figure 8: The performance of using the center frequency's coding pattern for the whole band.

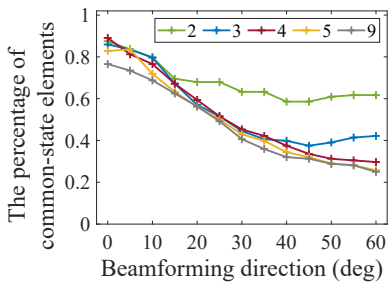

Figure 9: The ratio of the identical elements with different numbers of frequencies considered.

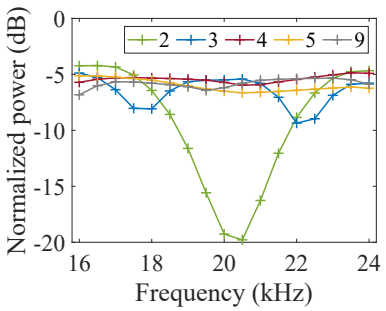

Figure 10: The power gain performance with different numbers of frequencies selected.

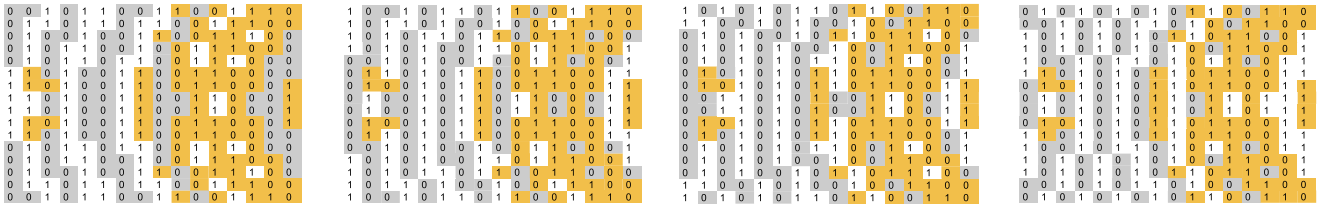

(a) 16 kHz **(b) 18 kHz** **(c) 21 kHz** **(d) 24 kHz**

Figure 11: The 1-bit coding patterns for different frequencies when the beamforming angle is set at 45 °. The common element states across these patterns are highlighted in yellow.

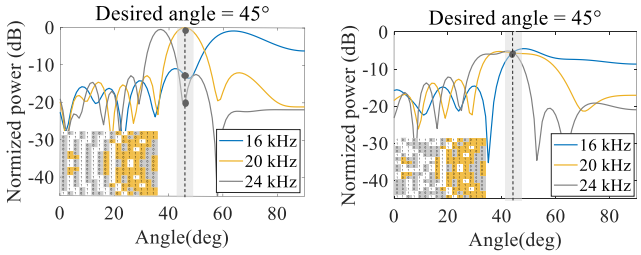

(a) Before optimization. **(b) After optimization.**

Figure 12: Simulated beam patterns before and after optimization.

Determine the number of frequencies considered for optimization. The number of frequencies considered is crucial, as it influences both computational load and the beamforming performance. Figure 9 shows the percentage of common-state elements varies with the number of frequencies optimized. In this simulation, we consider a total of 256 elements and various beamforming directions. The frequency range spans from 16 to 24 kHz, and we examine the effect of considering 2 to 9 frequencies. For each number of frequencies, we choose frequencies evenly distributed within the range. We observe that an increase in the number of selected frequencies leads to a decrease in the percentage of common-state elements and accordingly a larger computational cost. However, selecting too few frequencies cannot represent the entire frequency band, leading to fluctuations of beamforming gain among frequencies. As shown in Figure 10, selecting only 2-3 frequencies results in significant fluctuations in beamforming gain. Therefore, to maintain a balance between computational load and beamforming performance, we empirically choose 4 or 5 frequencies.

In summary, for wideband beamforming, we keep the common-state elements across multiple evenly distributed frequencies in the range and only optimize the states of the remaining elements using the PSO algorithm through minimizing the objective function in Equation 8. We present an example in Figure 12. As shown in Figure 12a, if we apply the optimal coding pattern at 20 kHz to 16 kHz and 24 kHz, there exists a noticeable gain drop at the desired angle (i.e., 45°). In contrast, as shown in Figure 12b, the proposed coding pattern $\boldsymbol{\Phi}^*$ achieves consistent high gain at all the three frequencies in a wide range. This is particularly meaningful for chirp signal widely adopted for sensing which spans across a relatively large frequency range.

5 IMPLEMENTATION

In this section, we present the implementation of the proposed acoustic metasurface and our experiment setup.

Metasurface fabrication. We fabricated the proposed configurable acoustic metasurface with 16×16 elements, using low-cost resin material [17] through 3D printing. Each element is designed with a side length of 1.1 cm, which is large enough to accommodate the off-the-shelf control components. Figure 13 shows the prototype of the metasurface, which has a size of $17.6 \times 17.6\ cm^2$. Within each element, we integrated a solenoid valve [41] with a unit price of \$0.3. The control components are connected to an FPGA controller board. The FPGA adopted in our design (Xilinx Artix-7

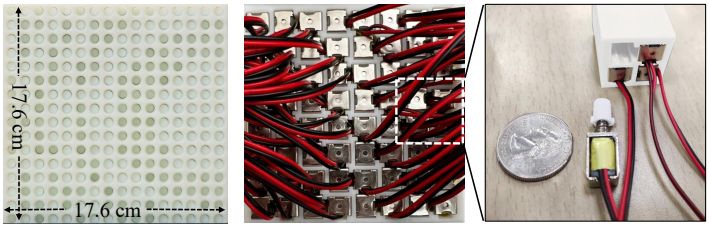

Figure 13: The prototype of CW-AcousLen.

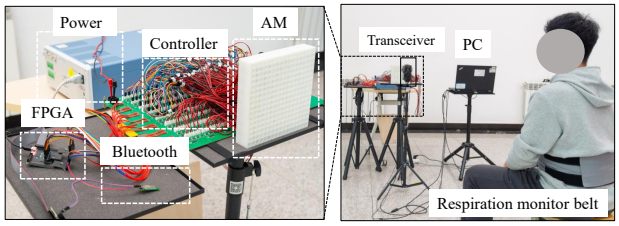

Figure 14: The system setup.

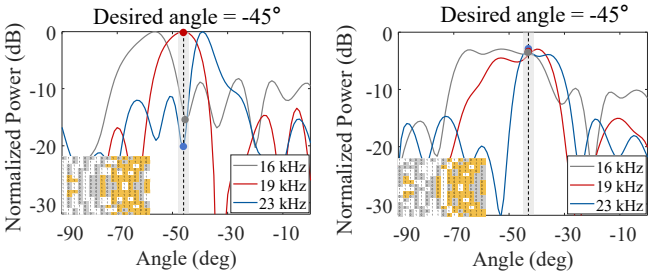

(a) Before optimization. **(b) After optimization.**

Figure 15: Experiment results of wideband beamforming.

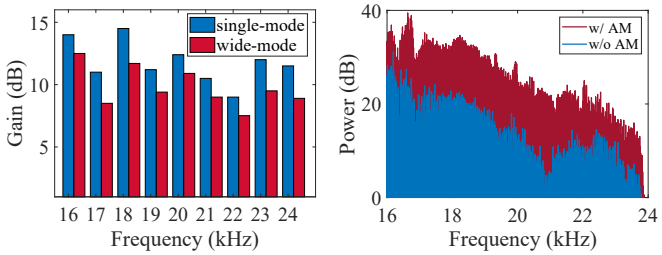

(a) Single vs. multiple frequency. **(b) FMCW signals.**

Figure 16: Performance of single-mode and wide-mode.

XC7A35T [14]) costs $60, and only 20% of the FPGA resource is used. Some lower-priced FPGAs are also feasible.

Experiment setup. We employ the experiment setup shown in Figure 14 for our evaluation. The setup includes three main components: speaker, microphone, and the proposed acoustic metasurface. In the controlled experiments detailed in Section 6.1, we use the proposed metasurface and a single speaker as the default equipment. The speaker is placed 0.2 m and 0.5 m in front of the metasurface. The microphone is placed 2 m from the metasurface in both scenarios. To calculate the sound pressure level (SPL), we record the sound signals using a high-end microphone (miniDSP UMIK-1 [34]) and then process them using the SPLmeter function in MATLAB. For setups that involve a speaker array, multiple speakers are connected to a Bela board [3] to ensure synchronization for beamforming. The coding pattern of the metasurface is then configured to further strengthen and redirect the beam produced by the speaker array.

Metasurface for Sensing. We evaluate the effectiveness of our acoustic metasurface on enhancing sensing performance through two representative sensing applications: (i) respiration monitoring and (ii) hand gesture recognition. For both applications, the transmitter transmits chirp signals (16-23 kHz) for sensing. We recruited 10 volunteers for our study. For respiration monitoring, each experiment trial lasted for 60 seconds and was repeated 5 times. We used a respiration monitor belt (NUL-236 [39]) to record ground truth data. For hand gesture recognition, we extracted channel impulse response (CIR) features and employed a neural network for training and classification. Each volunteer performed five different gestures, and we collected 30 samples per gesture at various positions. The data set was divided, with 80% used for training and the remaining 20% for testing. We use a camera to obtain the ground truth. We use respiration rate error and gesture recognition accuracy as the performance metrics.

Metasurface for communication. For communication, we implement Orthogonal Frequency-Division Multiplexing (OFDM) for data transmission. Specifically, each OFDM frame is composed of 180 Binary Phase Shift Keying (BPSK) symbols, distributed across 42 subcarriers within the frequency range of 16 to 23 kHz. We evaluate the communication performance in terms of Signal-to-Noise Ratio (SNR) and data rate.

6 EVALUATION

In this section, we conduct experiments to evaluate the performance of the proposed acoustic metasurface.

6.1 Benchmark Experiment

Wideband beamforming capability. This experiment compares the beamforming performance between directly using the center frequency's coding pattern and CW-AcousLen's optimized coding pattern for the frequency range of 16-23 kHz. We set the desired beamforming angle as 45°. To measure the beam pattern, we move the microphone around the metasurface following a 2 m radius arc, ranging from 0° to 90° at a step size of 5°, and record the sound pressure level at each position. Figure 15 shows that without the proposed wideband support, the coding pattern of the center frequency does not work well at other frequencies. The proposed wideband coding pattern can work at all frequencies with relatively high gains.

Performance of single-frequency mode and wideband mode. We validate the performance of the acoustic metasurface in both single-frequency and wideband modes. In this experiment, the speaker is positioned 0.2 m from the metasurface while the microphone is placed at a distance of 2 m. For the single-frequency mode, we transmit a sine wave with a frequency varying from 16 to 24 kHz. At each frequency, we configure the metasurface

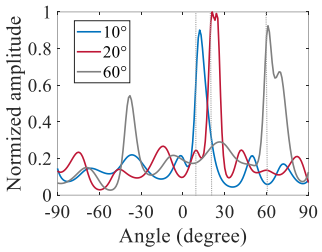

Figure 17: Beam pattern at different angles.

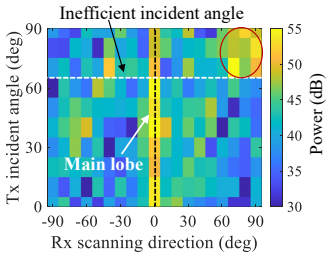

Figure 18: The performance of different incident angles.

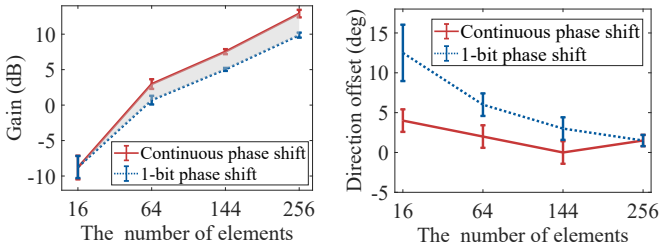

Figure 19: 1-bit phase shift vs. continuous phase shift.

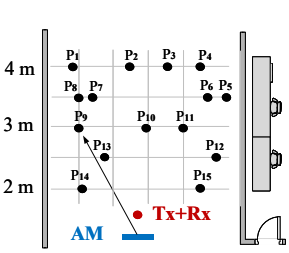

(a) LoS layout.

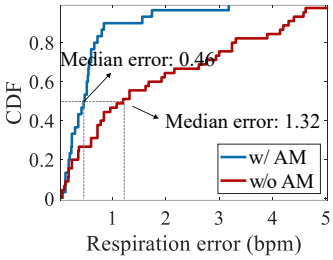

(b) Respiration rate monitoring.

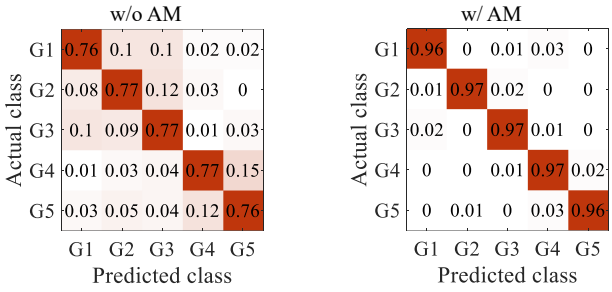

(c) Gesture recognition.

Figure 20: Acoustic sensing accuracy in LoS scenario.

using the corresponding single-frequency coding pattern. For the wideband mode, we evaluate the performance using both multiple single frequencies and FMCW chirp signals using the proposed wideband coding pattern. The results are illustrated in Figure 16. The improvements shown in Figure 16a are obtained by comparing to the baseline scenario without the metasurface. In FMCW chirp case, the proposed metasurface achieves relatively consistent gain over the whole ultrasonic frequency range. These results demonstrate that CW-AcousLen works well in both single-frequency and wideband modes.

Beam pattern at different beamforming angles. In this experiment, we keep the speaker-metasurface distance fixed at 0.2 m. To measure the beam pattern, we place the metasurface at the center of a circle with a radius of 2 m and measure the sound pressure level along this circle at a step size of 5°. We measure the beam pattern at three different beamforming directions, i.e., 10°, 20°, and 60°. Figure 17 shows the beam patterns at the three beamforming angles. The amplitude is normalized against the maximum received signal amplitude. We can see that the acoustic metasurface effectively creates directional beams, with the main lobe accurately pointing to the desired direction. While a side lobe is observed at -38 ° when the beamforming angle is 60°, it does not affect the amplitude and direction of the main lobe.

The effective incident angles. We conduct experiments to explore the effective range of incident angles. In these experiments, we vary the incident angle from 0° to 90°, while the desired beamforming direction (i.e., main lobe) is set as 0°. We measure the sound pressure level along a semicircle with a radius of 2 m, spanning from -90° to 90°. The results are shown in Figure 18. We can see that the metasurface can effectively beamform towards 0° even when the signal incident angle is 60°. However, when the incident angle is between 70° and 90°, the main lobe deviates from 0°, and strong side lobes appear. This is because when the signal incident angle is between 70° and 90°, the incident signal is nearly parallel to the metasurface, which is not effective for signal reflection. Therefore, we suggest to constrain the signal incident angle within 60° for best performance.

1-bit vs. continuous phase shift. In this experiment, we compare the performance between 1-bit (i.e., two states) phase shift and continuous phase shift under different sizes of metasurface (i.e., from 4×4 to 16×16 elements). The continuous phase shift metasurface is realized by constructing a non-configurable metasurface with a fixed beamforming direction at 20° using 3D printing technique. Figure 19 compares the gain difference and direction offset of the main lobe between continuous and 1-bit metasurfaces. We can see that 1) as the number of elements in the metasurface increases, the direction offset of the 1-bit phase shift decreases and eventually approaches zero. 2) The 1-bit phase shift configuration only results in a slight reduction of signal strength compared to the continuous phase shift. These experiment results align with the simulation results presented in Section 4.1.

6.2 Acoustic sensing performance

Performance in LoS scenarios. In this experiment, we evaluate the sensing performance of respiration monitoring and gesture recognition in LoS scenarios. The deployment is shown in Figure 20a. We randomly select 15 locations spanning various distances and angles. At each location, respiration monitoring lasts for 60 s and is repeated 5 times. For gesture recognition, the target performs five different gestures, i.e., G1—Push-Pull, G2—Swipe left

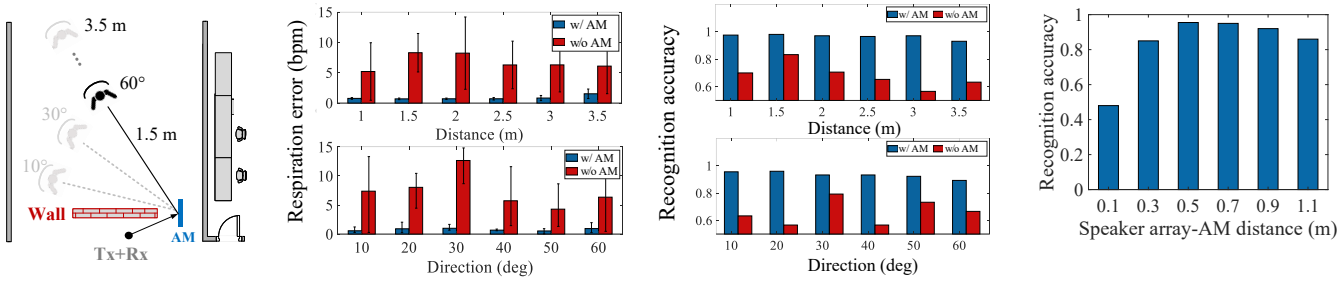

(a) NLoS layout. (b) Respiration rate monitoring. (c) Gesture recognition.

Figure 21: Acoustic sensing performance at different distances and directions in NLoS scenario.

Figure 22: Impact of distance between transmitter and metasurface.

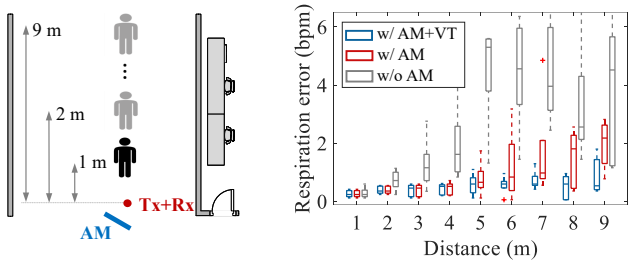

(a) Layout. (b) Respiration rate error.

Figure 23: The performance at different sensing distances.

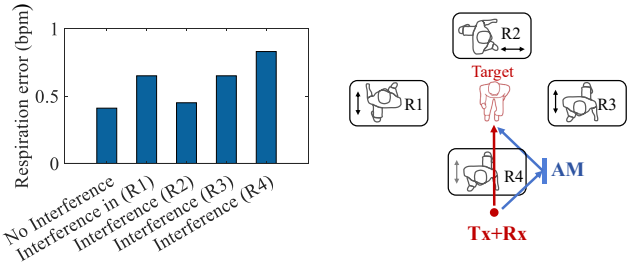

Figure 24: The capability of combating interference.

and right, G3—Move Clockwise, G4—Flick, and G5—Push forward. A total of 1500 gesture traces are collected at 15 locations. The overall performance is shown in Figure 20b and Figure 20c. We can see that, the median error of respiration rate sensing is reduced from 1.32 to 0.46 bpm (beats per minute) when the proposed metasurface is applied, and the average gesture recognition accuracy is increased from 76.67% to 96.67%. Note that the low gesture recognition accuracy (76.67%) without metasurface is mainly due to the large target-device distance/angle.

Performance in NLoS scenarios. We conduct experiments in NLoS scenarios when the path between the target and transceiver is blocked by a wall. The layout is shown in Figure 21a. The metasurface is placed 0.5 m away from the transceiver. The respiration rate error and gesture recognition accuracy are shown in Figure 21b and Figure 21c. We can see that when there is no metasurface, neither respiration nor gestures can be accurately sensed. This is because when the primary reflection (i.e., reflected once) is blocked, the secondary reflections (i.e., reflected twice or more) are too weak to be utilized for sensing. With the proposed acoustic metasurface, the accuracy for both respiration monitoring and gesture recognition is improved significantly. Even at a distance of 3 m from the metasurface, the error of respiration rate is still maintained below 1 bpm, and the gesture recognition accuracy is above 90%. These results demonstrate that the metasurface can redirect the incidental signal to cover areas occluded by obstacles, enabling acoustic sensing in NLoS scenarios.

The effect of transmitter-metasurface distance. The state-of-the-art [51] places a metasurface very close (i.e., 2 cm) to a speaker array to enable configurability. In this experiment, we investigate how the distance between the speaker array and metasurface affects sensing accuracy for our design. We conduct experiments in the NLoS scenario. We keep the metasurface 2 m away from the target and vary the distance between the speaker array and the metasurface from 0.1 m to 1.1 m. As shown in Figure 22, when the speaker array is too close to the metasurface, e.g., 0.1 m, both the direct path and metasurface path are blocked by the wall, leading to low recognition accuracy. By placing a metasurface relatively far away from the transmitter, e.g., more than 0.5 m, the metasurface path can be redirected to the target, significantly improving the recognition accuracy to higher than 95%. This result shows that the proposed metasurface design can work at a larger distance with respect to the transmitter to mitigate the issue of blockage.

The effect of target-metasurface distance. The deployment layout is shown in Figure 23a. In this experiment, we set the distance between the transceiver (co-located speaker and microphone) and the metasurface as 0.2 m. In Figure 23b, we compare the respiration sensing performance when using (refer to w/ AM) and not using metasurface (refer to w/o AM), as well as when combining metasurface with virtual transceiver (refer to w/ AM+VT) technique. The human target is positioned between 1 m and 9 m away from the transceiver. We observe that the performance is comparable when the target is within a range of 2 m. However, when the target is further away from the transceiver (i.e., larger than 4 m), the performance without the metasurface significantly degrades. We also note that even at a distance of 6 m, CW-AcousLen can still achieve a medium error lower than 1 bpm. The better performance benefits from the improved SNR brought by the proposed metasurface. By further combining the advanced signal processing technique,

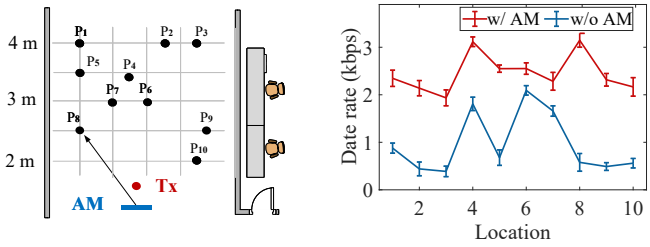

(a) Layout. (b) Date rate improvement

Figure 25: Wideband communication performance.

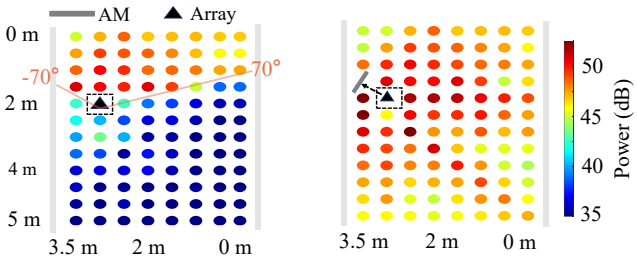

(a) Array (b) Acoustic metasurface + Array

Figure 26: Cooperation with a speaker array.

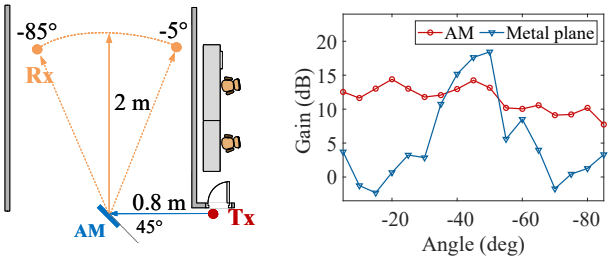

(a) Layout. (b) SNR improvement.

Figure 27: Metasurface vs. metal reflector.

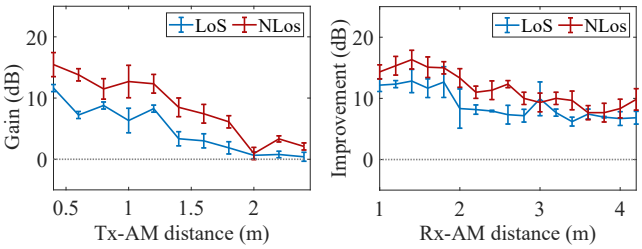

(a) SNR improvement. (b) SNR improvement.

Figure 28: The impact of transceiver-AM distance.

i.e., the virtual transceiver technique [24], the sensing distance is further increased to 8-9 m with a median error lower than 1 bpm.

Combating interference. We evaluate the performance of CW-AcousLen in the presence of dynamic interference, such as moving humans in the surrounding area. The experiment setup is shown in Figure 24 (right), where another individual moves near the target at location R1, R2, R3, and R4, respectively. As shown in Figure 24 (left), the respiration rate error slightly increases in the presence of such interference. The error at location R4 is slightly higher than those at other locations. Nevertheless, the respiration rate error remains below 1 bpm, demonstrating CW-AcousLen's robustness against interference. This resilience can be attributed to the metasurface's capability of creating directional beams. Such directional beamforming allows the transceiver to focus power at a specific target, mitigating environmental interference.

6.3 Acoustic communication performance

Concurrent wideband communication. In this experiment, we evaluate the performance of CW-AcousLen on improving acoustic communication using OFDM chirp signals spanning from 16 kHz to 23 kHz. We investigate the data rate improvement brought by CW-AcousLen's wideband beamforming capability. The deployment layout is shown in Figure 25a. We select 10 Rx locations spanning across various distances and angles. At each location, we collect 20 measurements and calculate the average data rate. The result is shown in Figure 25b. The average data rate is improved from 0.9 kbps to 2.41 kbps, which demonstrates CW-AcousLen's capability on improving channel gains for acoustic communication.

Collaborating with a speaker array. When combining a metasurface with a speaker array, we can employ the speaker array for beam steering or utilize the metasurface to re-direct the incident signal. This setup allows us to significantly extend the angle coverage. We conducted experiments in a $3.5 \times 5\ m^2$ hall and measured the signal power with and without the metasurface at various locations. The results are shown in Figure 26. We can see that the beamforming coverage of the speaker array with four speakers is constrained within a certain angular range, approximately $[-70°, 70°]$. By incorporating a metasurface, we can redirect the speaker's signal to cover those areas that the speaker array cannot cover. As shown in Figure 26b, the coverage can be effectively expanded to almost 360° through combining the speaker array with the metasurface.

Metasurface vs. metal reflector. In this experiment, we compare the performance of an ideal signal reflector, i.e., a metal plane and the proposed metasurface. As shown in Figure 27a, both the reflector and metasurface are placed 0.8 m from the transmitter with an incident angle of 45°. We vary the beamforming direction of the metasurface from -5° to -85° and measure the SNR at each direction for both the metasurface and the metal plane. The results are shown in Figure 27b. While the metal plane can create a strong main lobe at -45°, its signal strength drastically drops at other angles. In contrast, CW-AcousLen is able to achieve high gain across a much wider angular range.

Performance at different transceiver-metasurface distances. In this experiment, we evaluate how the distance between the transmitter/receiver and the metasurface affects performance in both LoS and NLoS scenarios. As shown in Figure 28, CW-AcousLen remains effective for enhancing SNR in both LoS and NLoS scenarios, even as the transceiver distance from the metasurface increases. Notably, the metasurface shows optimal performance when either the transmitter, receiver, or both are closer to it, with an effective

working distance exceeding 2 m for the transmitter and 4 m for the receiver. The average SNR improvements are 7.5 dB and 10.5 dB in LoS and NLoS scenarios, respectively. Furthermore, the improvement in SNR is more significant in NLoS scenarios compared to LoS scenarios.

7 DISCUSSION AND LIMITATION

The supported bandwidth. Our acoustic metasurface is currently designed for ultrasound frequency range, i.e., 16 - 24 kHz, suitable for sensing applications. The same design can be applied to lower frequency range by modifying the geometric parameters of the metasurface elements. However, for a frequency range with larger wavelength difference, it is more challenging to make the phase shift similar. For example, for the same 8 kHz working range, it is much more difficult to make 1-9 kHz band work than to make 16-24 kHz band work because the former band's maximum wavelength is 9 times larger than the minimum one while the later band is just 50% larger. On the other hand, designing a compact metasurface for even lower frequency range (e.g., 500 Hz to 1 kHz) remains challenging because the wavelength is much larger (i.e., meters) and the element size needs to be large to be efficient.

Multi-target sensing. To support simultaneous beamforming at multiple targets, we can create multi-beam patterns toward different targets. However, with multiple targets, the power focused at each target will unavoidably decrease. Another interesting observation is that when one lobe of the beamforming pattern is affected by target movement, the amplitudes of other lobes are also affected even without any target movement at the direction of other lobes. This brings an interesting research problem to differentiate between real target-induced lobe variation and algorithm-induced lobe variation.

8 CONCLUSION

In this paper, we present a wideband and configurable acoustic metasurface for the first time. Through careful hardware and software co-design, CW-AcousLencan support a wide inaudible band, i.e., 16 kHz - 24 kHz. Extensive experiments on sensing and communication demonstrate the effectiveness of proposed system in real-world environments. We believe the proposed designs can inspire follow-up research in this exciting area.

9 ACKNOWLEDGMENTS

This work is supported by the NSFC A3 Foresight Program under Grant 62061146001, and the National Natural Science Foundation of China under Grants (62272388, 62372372), Shaanxi Science and Technology Innovation Team Program under Grant 2024RS-CXTD-05, and Key Research and Development Program of Shaanxi under Grants (2024GH-ZDXM-46 and 2024GH-YBXM-08). We thank anonymous reviewers and the shepherd for their valuable feedback.

REFERENCES

[1] COMSOL Multiphysics 6.0. 2022. Simulate real-world designs, devices, and processes with multiphysics software from comsol. https://cn.comsol.com/
[2] Yang Bai, Nakul Garg, and Nirupam Roy. 2022. Spidr: Ultra-low-power acoustic spatial sensing for micro-robot navigation. In *Proceedings of the 20th Annual International Conference on Mobile Systems, Applications and Services*. 99–113.
[3] Bela. 2022. Bela: create beautiful interaction with sensors and sound. https://bela.io/
[4] Rachel Berkowitz. 2018. Acoustic metasurface creates quiet locations in a room. *Physics Today* 71, 8 (2018), 18–20.
[5] Shirui Cao, Dong Li, Sunghoon Ivan Lee, and Jie Xiong. 2023. PowerPhone: Unleashing the Acoustic Sensing Capability of Smartphones. In *Proceedings of the 29th Annual International Conference on Mobile Computing and Networking*. 1–16.
[6] W. K. Cao, C. Zhang, L. T. Wu, K. Q. Guo, and Q. Cheng. 2021. Tunable Acoustic Metasurface for Three-Dimensional Wave Manipulations. *Physical Review Applied* 15, 2 (2021).
[7] Lili Chen, Wenjun Hu, Kyle Jamieson, Xiaojiang Chen, Dingyi Fang, and Jeremy Gummeson. 2021. Pushing the Physical Limits of {IoT} Devices with Programmable Metasurfaces. In *18th USENIX Symposium on Networked Systems Design and Implementation (NSDI 21)*. 425–438.
[8] Xiangru Chen, Dong Li, Yiran Chen, and Jie Xiong. 2022. Boosting the sensing granularity of acoustic signals by exploiting hardware non-linearity. In *Proceedings of the 21st ACM Workshop on Hot Topics in Networks*. 53–59.
[9] Xing Chen, Peng Liu, Zewei Hou, and Yongmao Pei. 2017. Magnetic-control multifunctional acoustic metasurface for reflected wave manipulation at deep subwavelength scale. *Scientific reports* 7, 1 (2017), 1–9.
[10] Kun Woo Cho, Mohammad H Mazaheri, Jeremy Gummeson, Omid Abari, and Kyle Jamieson. 2021. mmWall: A reconfigurable metamaterial surface for mmWave networks. In *Proceedings of the 22nd International Workshop on Mobile Computing Systems and Applications*. 119–125.
[11] Manideep Dunna, Chi Zhang, Daniel Sievenpiper, and Dinesh Bharadia. 2020. ScatterMIMO: Enabling virtual MIMO with smart surfaces. In *Proceedings of the 26th Annual International Conference on Mobile Computing and Networking*. 1–14.
[12] Shi-Wang Fan, Sheng-Dong Zhao, A-Li Chen, Yan-Feng Wang, Badreddine Assouar, and Yue-Sheng Wang. 2019. Tunable broadband reflective acoustic metasurface. *Physical Review Applied* 11, 4 (2019), 044038.
[13] Chao Feng, Xinyi Li, Yangfan Zhang, Xiaojing Wang, Liqiong Chang, Fuwei Wang, Xinyu Zhang, and Xiaojiang Chen. 2021. RFlens: metasurface-enabled beamforming for IoT communication and sensing. In *Proceedings of the 27th Annual International Conference on Mobile Computing and Networking*. 587–600.
[14] Artix-7 Field Programmable Gate Array (FPGA). 2022. XC7A35T Xilinx A7. "https://docs.xilinx.com/v/u/en-US/ds181_Artix_7_Data_Sheet".
[15] Nakul Garg, Yang Bai, and Nirupam Roy. 2021. Owlet: Enabling spatial information in ubiquitous acoustic devices. In *Proceedings of the 19th Annual International Conference on Mobile Systems, Applications, and Services*. 255–268.
[16] Reza Ghaffarivardavagh, Sayed Saad Afzal, Osvy Rodriguez, and Fadel Adib. 2020. Ultra-wideband underwater backscatter via piezoelectric metamaterials. In *Proceedings of the Annual conference of the ACM Special Interest Group on Data Communication on the applications, technologies, architectures, and protocols for computer communication*. 722–734.
[17] Boedeker Plastics Inc. 2023. G-10 CR Cryogenic NP500CR Composite Sheet. https://www.boedeker.com/Product/G-10-CR-Cryogenic-NP500CR-Composite-Sheet Accessed: 2024.
[18] Texas Instruments. 2024. SN74HC595. https://www.ti.com.cn/product/cn/SN74HC595
[19] Richard Johnsonbaugh. 1998. A discrete intermediate value theorem. *The College Mathematics Journal* 29, 1 (1998), 42.
[20] James Kennedy and Russell Eberhart. 1995. Particle swarm optimization. In *Proceedings of ICNN'95-international conference on neural networks*, Vol. 4. IEEE, 1942–1948.
[21] Karsten Knobloch, Lars Enghardt, and Friedrich Bake. 2018. Helmholtz resonator liner with flexible walls. In *2018 AIAA/CEAS Aeroacoustics Conference*. 4102.
[22] Dong Li, Shirui Cao, Sunghoon Ivan Lee, and Jie Xiong. 2022. Experience: practical problems for acoustic sensing. In *Proceedings of the 28th Annual International Conference on Mobile Computing And Networking*. 381–390.
[23] Dong Li, Jialin Liu, Sunghoon Ivan Lee, and Jie Xiong. 2020. FM-track: pushing the limits of contactless multi-target tracking using acoustic signals. In *Proceedings of the 18th Conference on Embedded Networked Sensor Systems*. 150–163.
[24] Dong Li, Jialin Liu, Sunghoon Ivan Lee, and Jie Xiong. 2022. Lasense: Pushing the limits of fine-grained activity sensing using acoustic signals. *Proceedings of the ACM on Interactive, Mobile, Wearable and Ubiquitous Technologies* 6, 1 (2022), 1–27.
[25] Dong Li, Jialin Liu, Sunghoon Ivan Lee, and Jie Xiong. 2022. Room-Scale Hand Gesture Recognition Using Smart Speakers. In *Proceedings of the 20th ACM Conference on Embedded Networked Sensor Systems*. 462–475.
[26] Xinyi Li, Chao Feng, Fengyi Song, Chenghan Jiang, Yangfan Zhang, Ke Li, Xinyu Zhang, and Xiaojiang Chen. 2022. Protego: securing wireless communication via programmable metasurface. In *Proceedings of the 28th Annual International Conference on Mobile Computing And Networking*. 55–68.
[27] Xinyi Li, Chao Feng, Xiaojing Wang, Yangfan Zhang, Yaxiong Xie, and Xiaojiang Chen. 2023. {RF-Bouncer}: A Programmable Dual-band Metasurface for Sub-6 Wireless Networks. In *20th USENIX Symposium on Networked Systems Design and Implementation (NSDI 23)*. 389–404.
[28] Xinwei Li, Xiang Yu, Jun Wei Chua, and Wei Zhai. 2023. Harnessing cavity dissipation for enhanced sound absorption in Helmholtz resonance metamaterials.

Materials Horizons (2023).
[29] Y. Li, B. Liang, Z. M. Gu, X. Y. Zou, and J. C. Cheng. 2013. Reflected wavefront manipulation based on ultrathin planar acoustic metasurfaces. *Rep* 3 (2013).
[30] Jialin Liu, Dong Li, Lei Wang, Fusang Zhang, and Jie Xiong. 2022. Enabling Contact-free Acoustic Sensing under Device Motion. *Proceedings of the ACM on Interactive, Mobile, Wearable and Ubiquitous Technologies* 6, 3 (2022), 1–27.
[31] Guancong Ma, Xiying Fan, Ping Sheng, and Mathias Fink. 2018. Shaping reverberating sound fields with an actively tunable metasurface. *Proceedings of the National Academy of Sciences* 115, 26 (2018), 6638–6643.
[32] Ruichun Ma, R Ivan Zelaya, and Wenjun Hu. 2023. Softly, Deftly, Scrolls Unfurl Their Splendor: Rolling Flexible Surfaces for Wideband Wireless. *arXiv preprint arXiv:2306.02361* (2023).
[33] Wenguang Mao, Mei Wang, Wei Sun, Lili Qiu, Swadhin Pradhan, and Yi-Chao Chen. 2019. Rnn-based room scale hand motion tracking. In *The 25th Annual International Conference on Mobile Computing and Networking*. 1–16.
[34] miniDSP. 2022. miniDSP UMIK-1: USB Measurement Microphone. https://www.minidsp.com/products/acoustic-measurement/umik-1
[35] Yao-Yin Peng, Jin-Heng Chen, Zhang-Zhao Yang, Xin-Ye Zou, Chao Tao, and Jian-Chun Cheng. 2022. Broadband tunable acoustic metasurface based on piezoelectric composite structure with two resonant modes. *Applied Physics Express* 15, 1 (2022), 014004.
[36] Yao-Yin Peng, Zhang-Zhao Yang, Zhi-Lei Zhang, Xin-Ye Zou, Chao Tao, and Jian-Chun Cheng. 2022. Tunable acoustic metasurface based on tunable piezoelectric composite structure. *The Journal of the Acoustical Society of America* 151, 2 (2022), 838–845.
[37] Kun Qian, Lulu Yao, Xinyu Zhang, and Tse Nga Ng. 2022. MilliMirror: 3D printed reflecting surface for millimeter-wave coverage expansion. In *Proceedings of the 28th Annual International Conference on Mobile Computing And Networking*. 15–28.
[38] Hamid Rajabalipanah, Mohammad Hosein Fakheri, and Ali Abdolali. 2020. Electromechanically programmable space-time-coding digital acoustic metasurfaces. *arXiv preprint arXiv:2003.12616* (2020).
[39] Neulog NUL236 Respiration Monitor Belt Logger Sensor. 2022. NUL-236. "https://www.amazon.com/NEULOG-Respiration-Monitor-Resolution-Maximum/dp/B00B76OZ9I".
[40] C. Shen and Steven A Cummer. 2018. Harnessing Multiple Internal Reflections to Design Highly Absorptive Acoustic Metasurfaces. *Physical Review Applied* 9, 5 (2018), 054009.
[41] Mini DC Solenoid. 2022. https://www.aliexpress.us/item/2255800185149158.html?spm=a2g0o.detail.1000023.1.2dc23cf8OnWyRM&gatewayAdapt=glo2usa4itemAdapt&_randl_shipto=US.
[42] Xinpei Song, Tianning Chen, Weikang Huang, and Chen Chen. 2021. Frequency-selective modulation of reflected wave fronts using a four-mode coding acoustic metasurface. *Physics Letters A* 394 (2021), 127145.
[43] Zhaoyong Sun, Yu Shi, Xuecong Sun, Han Jia, Zhongkun Jin, Ke Deng, and Jun Yang. 2021. Underwater acoustic multiplexing communication by pentamode metasurface. *Journal of Physics D: Applied Physics* 54, 20 (2021), 205303.
[44] Haoran Wan, Shuyu Shi, Wenyu Cao, Wei Wang, and Guihai Chen. 2021. RespTracker: Multi-user room-scale respiration tracking with commercial acoustic devices. In *IEEE INFOCOM 2021-IEEE Conference on Computer Communications*. IEEE, 1–10.
[45] Rui Wang and Fengbao Yang. 2022. Acoustic reflected wavefront modulation based on Helmholtz resonator array. *AIP Advances* 12, 11 (2022), 115314.
[46] Kai Wu, Jing-Jing Liu, Yu-jiang Ding, Wei Wang, Bin Liang, and Jian-Chun Cheng. 2022. Metamaterial-based real-time communication with high information density by multipath twisting of acoustic wave. *Nature communications* 13, 1 (2022), 5171.
[47] Dianhan Xie, Xudong Wang, and Aimin Tang. 2022. Metasight: Localizing blocked rfid objects by modulating nlos signals via metasurfaces. In *Proceedings of the 20th Annual International Conference on Mobile Systems, Applications and Services*. 504–516.
[48] Sangki Yun, Yi-Chao Chen, Huihuang Zheng, Lili Qiu, and Wenguang Mao. 2017. Strata: Fine-grained acoustic-based device-free tracking. In *Proceedings of the 15th annual international conference on mobile systems, applications, and services*. 15–28.
[49] Ali Zabihi, Chadi Ellouzi, and Chen Shen. 2023. Tunable, reconfigurable, and programmable acoustic metasurfaces: A review. *Frontiers in Materials* 10 (2023), 1132585.
[50] Lei Zhang, Ming Zheng Chen, Wankai Tang, Jun Yan Dai, Long Miao, Xiao Yang Zhou, Shi Jin, Qiang Cheng, and Tie Jun Cui. 2021. A wireless communication scheme based on space-and frequency-division multiplexing using digital metasurfaces. *Nature electronics* 4, 3 (2021), 218–227.
[51] Yongzhao Zhang, Yezhou Wang, Lanqing Yang, Mei Wang, Yi-Chao Chen, Lili Qiu, Yihong Liu, Guangtao Xue, and Jiadi Yu. 2023. Acoustic Sensing and Communication Using Metasurface. In *20th USENIX Symposium on Networked Systems Design and Implementation (NSDI 23)*. 1359–1374.
[52] Yifan Zhu and Badreddine Assouar. 2019. Multifunctional acoustic metasurface based on an array of Helmholtz resonators. *Physical review B* 99, 17 (2019), 174109.
[53] Y. Zhu, X. Fan, B. Liang, J. Cheng, and Y. Jing. 2017. Ultra-thin Acoustic Metasurface-Based Schroeder Diffuser. *Phys.rev.x* 7, 2 (2017).
[54] Yifan Zhu, Xudong Fan, Bin Liang, Jianchun Cheng, and Yun Jing. 2017. Ultrathin acoustic metasurface-based Schroeder diffuser. *Physical Review X* 7, 2 (2017), 021034.
[55] Yifan Zhu, Jie Hu, Xudong Fan, Jing Yang, Bin Liang, Xuefeng Zhu, and Jianchun Cheng. 2018. Fine manipulation of sound via lossy metamaterials with independent and arbitrary reflection amplitude and phase. *Nature communications* 9, 1 (2018), 1–9.